

# Water cavitation results from the kinetic competition of bulk, surface and surface-defect nucleation events

Philip Loche,<sup>1,2</sup> Matej Kanduč,<sup>3</sup> Emanuel Schneck,<sup>4</sup> and Roland R. Netz

<sup>1</sup>*Laboratory of Computational Science and Modeling, IMX, École Polytechnique Fédérale de Lausanne, 1015 Lausanne, Switzerland*

<sup>2</sup>*Fachbereich Physik, Freie Universität Berlin, 14195 Berlin, Germany*

<sup>3</sup>*Department of Theoretical Physics, Jožef Stefan Institute, 1000 Ljubljana, Slovenia*

<sup>4</sup>*Physics Department, Technische Universität Darmstadt, 64289 Darmstadt, Germany*

(\*Electronic mail: rnetz@physik.fu-berlin.de)

Water at negative pressures can remain in a metastable state for a surprisingly long time before it reaches equilibrium by cavitation, i.e. by the formation of vapor bubbles. The wide spread of experimentally measured cavitation pressures depending on water purity, surface contact angle and surface quality implicates the relevance of water cavitation in bulk, at surfaces and at surface defects for different systems. We formulate a kinetic model that includes all three different cavitation pathways and determine the needed nucleation attempt frequencies in bulk, at surfaces and at defects from atomistic molecular dynamics simulations. Our model reveals that cavitation occurs in pure bulk water only for defect-free hydrophilic surfaces with wetting contact angles below  $50^\circ$  to  $60^\circ$  and at pressures of the order of  $-100$  MPa, depending only slightly on system size and observation time. Cavitation on defect-free surfaces occurs only for higher contact angles, with the typical cavitation pressure rising to about  $-30$  MPa for very hydrophobic surfaces. Nanoscopic hydrophobic surface defects act as very efficient cavitation nuclei and can dominate the cavitation kinetics in a macroscopic system. In fact, a nanoscopic defect that hosts a pre-existing vapor bubble can raise the critical cavitation pressure much further. Our results explain the wide variation of experimentally observed cavitation pressures in synthetic and biological systems and highlight the importance of surface and defect mechanisms for the nucleation of metastable systems.

## I. INTRODUCTION

When water is brought into a metastable state by either heating or pressure reduction, it will eventually reach equilibrium by cavitation, i.e., by the nucleation of vapor bubbles. Cavitation and the collapse of cavitation bubbles are central to applications such as inkjet printing, ultrasonic cleaning, noninvasive destruction of kidney stones by acoustic shockwaves, sonochemistry, sonoluminescence<sup>1,2</sup> and for the investigation of geothermal processes<sup>3</sup>. In contrast, the collapse of hydrodynamically produced cavitation bubbles has adverse effects on hydraulic systems, valves, and propeller blades, causing wear and erosion<sup>4-6</sup>, while the creation of cavitation bubbles may impact the performance of hydrofoils<sup>7</sup>. In biology, where temperature is fixed by the environment, metastable water is primarily produced by pressure reduction. The collapse of these cavitation bubbles provides catapult-like mechanisms in ferns<sup>8</sup> and allows snapping shrimp to stun their prey<sup>9</sup>. Conversely, cavitation limits the negative pressure produced by octopus suckers<sup>10</sup> and must be avoided in the ascending sap of tall trees, where significantly negative pressures are encountered, in importantly, metastable water at negative pressures can persist over astonishingly long times and cavitation occurs at experimentally relevant time scales only when the pressure sinks below a threshold cavitation pressure  $p_{\text{cav}}$ . The large variation of  $p_{\text{cav}}$  among different systems and its dependence on surface properties suggests that cavitation in bulk water (i.e., homogeneous nucleation) competes with cavitation on surfaces

and with cavitation at surface defects (i.e., heterogeneous nucleation). Understanding the kinetic competition between these three different cavitation pathways is important for all the above-mentioned applications and is the central theme of this paper.

Cavitation is a typical nucleation phenomenon; according to Classical Nucleation Theory (CNT), its kinetics is determined by the thermally activated stochastic crossing of a free energy barrier characteristic of the critical nucleus size<sup>11</sup>. CNT predicts that clean water at room temperature can sustain negative pressures considerably below  $-100$  MPa before bulk cavitation sets in<sup>2,12-15</sup>. This very low cavitation pressure predicted for clean bulk water is largely due to the high water surface tension. Experimentally, cavitation pressures below  $-100$  MPa have only been reached with ultra-clean water in microscopic quartz cavities<sup>16-18</sup>. In typical experiments with hydrophilic surfaces and using rigorous purification and degassing methods, cavitation pressures of the order of  $p_{\text{cav}} \approx -30$  MPa<sup>2,14,19</sup> are reached, significantly above the CNT results for clean bulk water. However, with untreated ordinary water in standard containers, the cavitation pressure is positive and typically only slightly below the saturated water vapor pressure of about 2 kPa. The consensus in the field is that surface cavitation at container walls, microscopic impurities<sup>20-26</sup>, surface imperfections, or crevices hosting pre-existing vapor or gas bubbles<sup>27-30</sup> act as cavitation nuclei. These nuclei promote cavitation and contribute to deviations in cavitation pressures from those predicted by CNT for clean bulk water.

These experimental complications make theoretical and simulation approaches essential. Molecular dynamics (MD) simulations with all-atom force fields have proven to be powerful tools for investigating cavitation processes<sup>31–34</sup>. Recent MD studies demonstrated that while dissolved gas has a negligible effect on cavitation thresholds<sup>35,36</sup>, gas nanobubbles can significantly promote cavitation<sup>26,37</sup>. Indeed, our recent MD study demonstrated that nonsoluble impurities in the form of nanodroplets suspended in water considerably increase cavitation pressures<sup>38</sup>. Another simulation study has shown that solid particles in water can disrupt the hydrogen-bond network and facilitate cavitation in small simulation volumes<sup>39</sup>. Despite these advances, the influence of specific surface properties on cavitation in macroscopic systems remains poorly understood, and a unified framework encompassing bulk, surface, and defect-induced cavitation is still missing.

In this work, we bridge this gap by formulating a kinetic cavitation model that combines MD simulations with the CNT framework. With attempt rates obtained from simulations, our kinetic model predicts the cavitation pressure,  $p_{\text{cav}}$ , of water confined in a cubic container, with walls characterized by the water contact angle. The model also incorporates various surface defect patches with distinct wetting properties. We find that for highly hydrophilic, defect-free surfaces, cavitation occurs in bulk water at pressures consistent with CNT predictions. As the surface contact angle increases beyond a critical threshold of  $50^\circ - 60^\circ$ , cavitation shifts to the surface. Finally, for surfaces with hydrophobic defects our comprehensive model provides a unified framework to understand and predict cavitation behavior in diverse practically relevant scenarios.

## II. MATERIALS AND METHODS

### Simulation model

The simulation setup follows our previous approach<sup>40,41</sup> and is shown in Fig. 1. We model a planar surface composed of two self-assembled monolayers, each consisting of ten-carbon-atom alkyl chains terminated by polar a hydroxyl (OH) head group. These hydroxylated alkanes are arranged on a hexagonal lattice with an areal density of  $4.3 \text{ nm}^{-2}$ . To stabilize the structure, we apply harmonic restraints to the second carbon atom from the head group with strengths of  $k_x = k_y = 500 \text{ (kJ/mol) nm}^{-2}$  in the lateral directions, and to the tenth (terminal) carbon atom with  $k_x = k_y = 10 \text{ (kJ/mol) nm}^{-2}$  laterally and  $k_z = 100 \text{ (kJ/mol) nm}^{-2}$  in the normal direction. The surface polarity and thereby the surface contact angle is controlled by scaling the partial charges of the head groups with a factor  $\alpha$ , ranging from 0 to 1. For  $\alpha = 0$ , the surface is non-polar with head groups resembling methylated termini, resulting in a contact

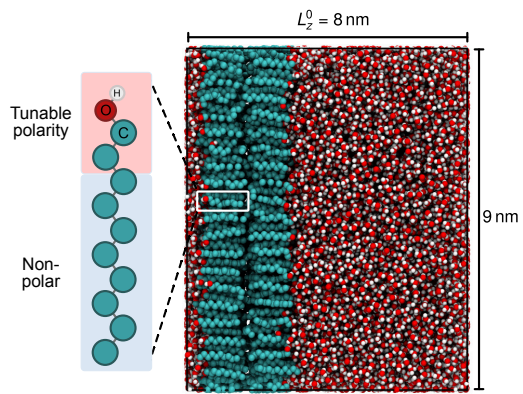


Figure 1. Simulation setup consisting of 800 surface molecules (hydroxylated alkanes) assembled into two self-assembled monolayers and solvated by 16,353 water molecules. Each surface molecule consists of an alkyl chain terminated by a modified hydroxyl group with its partial charges scaled by a factor  $\alpha$ . Simulation box (black frame) is replicated in all three directions via periodic boundary conditions. The box length for the initial pressure of  $-30 \text{ MPa}$  in the normal direction is  $L_z^0 = 8 \text{ nm}$ .

angle of  $\theta = 135^\circ$ . For  $\alpha = 1$ , the surface is fully polar, mimicking hydroxyl head groups. In the Supplementary Material, section S1, we present a phenomenological fit function that maps the surface polarity  $\alpha$  to the contact angle  $\cos \theta$ . The periodic simulation box, with initial dimensions  $9 \text{ nm} \times 10.4 \text{ nm} \times 8 \text{ nm}$  at a pressure of  $-30 \text{ MPa}$ , contains 16,353 water molecules and 800 hydroxylated alkanes.

We use united-atom parameters from the GROMOS force field for the alkanes<sup>41,42</sup> and the rigid SPC/E water model<sup>43</sup>. Classical non-polarizable molecular dynamics simulations are performed with the GROMACS package<sup>44</sup> using a time step of 2 fs. A plain cutoff of 0.9 nm is used for short-range Lennard-Jones interactions. Electrostatics is treated with the Smooth Particle–Mesh Ewald method, using a 0.9 nm real-space cutoff. A temperature of 300 K is controlled using the velocity rescale thermostat with a stochastic factor<sup>45</sup> and a time constant of 0.5 ps. Pressure is controlled by the Berendsen barostat with a time constant of 1 ps, suitable even for negative pressures because of its efficiency and stability in box scaling under large pressure differences. We previously verified<sup>36</sup> that equivalent results are obtained with the Parrinello–Rahman barostat, which more accurately reproduces volume fluctuations. Reference coordinates for surface-atom restraints are scaled with the coupling matrix of the pressure coupling.

### Kinetic theory for pressure ramps

To obtain the cavitation attempt frequencies, we use the pressure-ramp simulation protocol<sup>36</sup>, where the negative pressure decreases linearly over time as  $p(t) = \dot{p}t$  at

a constant rate  $\dot{p} < 0$ . To simulate pressure ramps, we conduct a sequence of simulations at constant pressures, starting from an initial pressure of  $-30$  MPa. After each simulation, the final coordinates are used to start the next simulation, with the pressure reduced by  $0.1$  MPa. The duration of each constant-pressure simulation depends on the pressure rate  $\dot{p}$ . We identify cavitation when the simulation box length  $L_z$  increases by more than  $50\%$  of its initial value  $L_z^0$ . The corresponding ‘‘dynamic’’ cavitation pressure  $p_{\text{cav}}^*$  follows from the solution of the linear cavitation rate equation as

$$p_{\text{cav}}^* = \dot{p} \int_0^\infty e^{-k_0 I(t)} dt, \quad (1)$$

where

$$I(t) = \int_0^t e^{-\beta G^*(t')} dt'. \quad (2)$$

Here,  $\beta = 1/k_B T$  is the inverse thermal energy, and  $G^*(t)$  is the time-dependent free energy barrier in the pressure-ramp protocol. According to CNT, this barrier decays with time as  $G^*(t) \sim t^{-2}$ . The attempt frequencies for bulk and surface cavitation,  $\kappa_{3\text{D}}$  and  $\kappa_{2\text{D}}$ , are obtained from fits of Eq. 1 to the simulation data; detail are given in the Supplementary Material, section S2.

### III. RESULTS AND DISCUSSION

#### A. Kinetic model for cavitation in water confined by surfaces with defects

In the typical cavitation scenario, as studied in this work, water is confined by solid surfaces with a given contact angle that contain a finite number of surface defects. Upon application of a negative pressure, cavitation can proceed in bulk, at the defect-free surface parts or at the defects. Since we cannot presuppose the prevalence of one cavitation pathway over the others, we write the total cavitation rate as the sum of the bulk (3D), surface (2D) and defect (def) rates as

$$k_{\text{tot}} = k_{3\text{D}} + k_{2\text{D}} + N_{\text{def}} k_{\text{def}}, \quad (3)$$

where  $N_{\text{def}}$  is the number of identical surface defects. The model assumes that the different cavitation pathways do not interfere with each other. It will turn out that depending on the surface and defect properties, quantified by their respective contact angles, one cavitation pathway will always dominate strongly over the other pathways, such that we can construct effective kinetic phase diagrams that feature regions where bulk, surface or defect cavitation dominates.

#### B. Cavitation in bulk

CNT is a general framework for the description of cavitation<sup>11</sup>. For cavitation in bulk, one considers a spherical

vapor bubble in a liquid with a free energy given by<sup>2,15,46</sup>

$$G_{3\text{D}} = 4\pi r^2 \gamma + \frac{4}{3} \pi r^3 p, \quad (4)$$

where  $\gamma$  is the liquid–vapor surface tension,  $r$  the bubble radius and  $p < 0$  the negative pressure in the liquid. The first term represents the bubble surface free energy and the second term the work associated with the volume expansion. We have neglected the saturated vapor pressure, which is irrelevant compared to the large magnitude of cavitation pressures considered here. For simplicity, we have also neglected curvature effects on the surface tension, which only introduce minor corrections<sup>31,36</sup>. The interplay between the two terms in Eq. 4 creates a free energy barrier for  $p < 0$  of

$$G_{3\text{D}}^* = \frac{16\pi}{3} \frac{\gamma^3}{p^2}, \quad (5)$$

reached at the critical bubble radius  $r^* = -2\gamma/p$  defined by  $dG_{3\text{D}}/dr|_{r=r^*} = 0$ . If a bubble surpasses the critical radius  $r^*$ , it will grow further and cause cavitation.

Cavitation can occur anywhere in bulk, its rate therefore is proportional to the liquid volume  $V$  and can be written as

$$k_{3\text{D}} = V \kappa_{3\text{D}} e^{-\beta G_{3\text{D}}^*}. \quad (6)$$

The cavitation time follows from the rate as  $\tau = k_{3\text{D}}^{-1}$  and is the mean time one has to wait for cavitation to occur. The exponential factor in Eq. 6 reflects the Arrhenius law<sup>47</sup>. The pre-exponential factor splits into the volume  $V$  and the attempt frequency density  $\kappa_{3\text{D}}$ , which is an intensive property of the liquid that characterizes the barrier-less cavitation rate. It thus constitutes the cavitation speed limit, i.e., the maximum rate at which cavitation occurs in the absence of a barrier<sup>48</sup>. The attempt frequency density,  $\kappa_{3\text{D}}$ , accounts for viscosity and hydrodynamic memory effects in the surrounding liquid, as well as for corrections to CNT, such as the curvature dependence of the interfacial tension<sup>49</sup>. Given the exponential dependence of the cavitation time  $\tau$  on  $p$ , it is preferred to consider the inverse relation. For a cubic volume  $V = L^3$ , the cavitation pressure follows from Eqs. 5 and 6 as<sup>2,50</sup>

$$p_{3\text{Dcav}}^2 = \frac{16\pi\gamma^3}{3k_B T} \frac{1}{\ln(\kappa_{3\text{D}} L^3 \tau)}. \quad (7)$$

It is seen that  $p_{3\text{Dcav}}$  depends only logarithmically and thus rather weakly on system size  $L$  and cavitation time  $\tau$ . Various methods for determining  $\kappa_{3\text{D}}$  have been proposed<sup>51,52</sup>. In a previous simulation study on bulk cavitation, we determined  $\kappa_{3\text{D}} = 5 \times 10^{11} \text{ ns}^{-1} \text{ nm}^{-3}$  for the SPC/E water model<sup>36</sup>, this value will be employed in the current study. Using the same water model and the same methodology ensures consistency and enables a direct comparison between bulk, surface and defect cavitation rates. It is noteworthy that CNT (as given

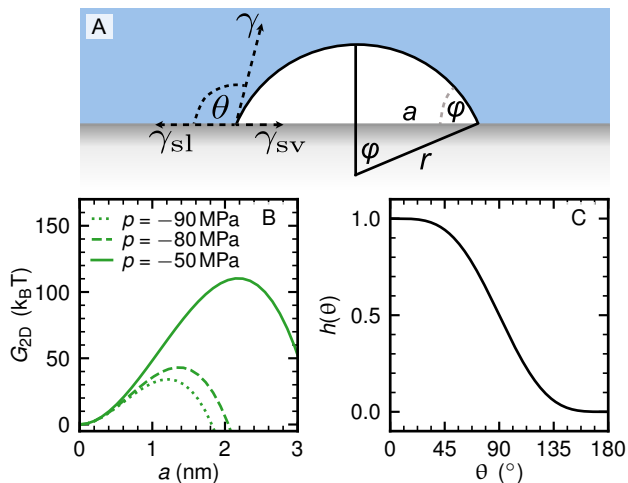


Figure 2. (A) Schematics of bubble cavitation on a surface. Bubble contact angle  $\varphi$  and water contact angle  $\theta$  are related by  $\varphi = \pi - \theta$ . (B) Free energy  $G_{2D}$  of a bubble on a surface with a contact angle of  $\theta = 97^\circ$  as a function of the bubble base radius  $a$  from Eq. 8 for various negative pressures  $p$ . (C) Geometric factor  $h(\theta) = G_{2D}^*/G_{3D}^*$  in Eq. 10.

by Eq. 7) for SPC/E water predicts  $p_{3Dcav}$  values from  $-80$  to  $-100$  MPa for  $L$  between  $1 \mu\text{m}$  and  $1 \text{m}$  and  $\tau = 1 \text{s}$ . This value is slightly higher than previous predictions, primarily because the surface tension of SPC/E water ( $\gamma_{\text{SPC/E}} \approx 55 \text{ mN/m}$  for a Lennard-Jones cutoff  $0.9 \text{ nm}^{41}$ ) is lower than the experimental value  $\gamma_{\text{exp}} = 72 \text{ mN/m}$ . Applying a correction factor of  $(\gamma_{\text{exp}}/\gamma_{\text{SPC/E}})^{3/2} \approx 1.5$  on  $p_{3Dcav}$ , as suggested by Eq. 7, yields good agreement with previous predictions<sup>2,12-15</sup>. We here stick to the SCP/E water model because it reproduces most dynamic water properties quite well.

Experimental validation of the CNT bulk cavitation prediction for water is challenging, as the bulk cavitation pathway is preempted by diverse surface and defect cavitation pathways. Nevertheless, bulk cavitation occurs in liquids with considerably lower surface tensions, such as hydrocarbons. With surface tensions approximately three times smaller than water, the predicted cavitation pressures by CNT (Eq. 7) are reduced by a factor of  $3^{3/2} \approx 5$ , resulting in cavitation pressures of  $-20$  to  $-30$  MPa. This range agrees well with experimentally measured cavitation pressures in various organic liquids<sup>53-56</sup>, providing validation of the CNT framework for bulk cavitation.

### C. Cavitation at a smooth defect-free surface

To apply the CNT framework, we write the free energy of a bubble at a surface, illustrated in Fig. 2 A, as

$$G_{2D} = A_{\text{cap}}\gamma + A_{\text{base}}(\gamma_{\text{sv}} - \gamma_{\text{sl}}) + pV_b, \quad (8)$$

where  $A_{\text{cap}} = 2\pi r^2(1 - \cos\varphi)$  is the area of the spherical bubble cap with radius of curvature  $r$ ,  $A_{\text{base}} = \pi a^2$  is the base area of the bubble with base radius  $a$  and  $V_b = (\pi/3)r^3(2 - 3\cos\varphi + \cos^3\varphi)$  is the bubble volume,  $\gamma_{\text{sv}}$  and  $\gamma_{\text{sl}}$  correspond to the solid-vapor and solid-liquid surface tensions, respectively, and  $\varphi$  is the contact angle of the bubble. Similar to Eq. 4, the first two terms account for the free energy of creating the bubble surface and the third term is the work associated with volume expansion. We neglect the buoyancy force, as it is irrelevant for determining the critical bubble size, which is on the nanometer scale, and mostly important for the pinching-off of full-grown bubbles.

Using Young's equation,  $\gamma_{\text{sv}} - \gamma_{\text{sl}} = \gamma \cos\theta$ , and the relation between the water contact angle  $\theta$  and the bubble contact angle  $\varphi$ ,  $\varphi + \theta = 180^\circ$ , we show in Fig. 2 B the free energy of a bubble at a hydrophobic surface characterized by a water contact angle  $\theta = 97^\circ$  according to Eq. 8 as a function of the base radius  $a$  for various pressures. The critical bubble size follows from  $dG_{2D}/da|_{a=a^*} = 0$  as  $a^* = -(2\gamma/p)\sin\theta$ , the corresponding radius of curvature is  $r^* = -2\gamma/p$ , as for homogeneous cavitation. The free energy barrier follows as

$$G_{2D}^*(\theta) = G_{3D}^* h(\theta), \quad (9)$$

which is reduced compared to the bulk result  $G_{3D}^*$  in Eq. 5 by the geometric factor<sup>2,11,22</sup>

$$h(\theta) = (2 - \cos\theta) \cos^4(\theta/2) \quad (10)$$

depicted in Fig. 2 C. For a completely wetting surface,  $\theta = 0$ , we find  $h(0) = 1$ , the bubble is detached from the surface and the bulk cavitation result is recovered. The factor  $h(\theta)$  decreases as the contact angle increases, ultimately disappearing for  $\theta = 180^\circ$ . The surface cavitation rate is written as

$$k_{2D} = A\kappa_{2D}(\theta) e^{-\beta G_{2D}^*(\theta)} \quad (11)$$

and is proportional to the total surface area  $A$ , where  $\kappa_{2D}$  is the attempt frequency surface density, which depends on the surface type and thus on the contact angle  $\theta$ . For the total surface area of a cubic container  $A = 6L^2$  and neglecting edge and corner effects, the surface cavitation pressure is given by

$$p_{2Dcav}^2 = \frac{16\pi\gamma^3}{3k_B T} \frac{h(\theta)}{\ln[\kappa_{2D}(\theta) 6L^2 \tau]}. \quad (12)$$

To determine  $\kappa_{2D}$  from simulations, we use a self-assembled monolayer of alkyl molecules terminated by headgroups with adjustable electric dipole moments<sup>40,41</sup>. The dipole moment controls the wetting characteristics of the surfaces. We examine six different dipole moments, resulting in contact angles of  $\theta = 45^\circ, 60^\circ, 76^\circ, 97^\circ, 120^\circ$  and  $135^\circ$ , on surfaces measuring  $9 \text{ nm} \times 10.4 \text{ nm}$  in contact with water. Obtaining the cavitation time from simulations at constant negative pressure is impractical due to the excessive waiting time for cavitation to occur.

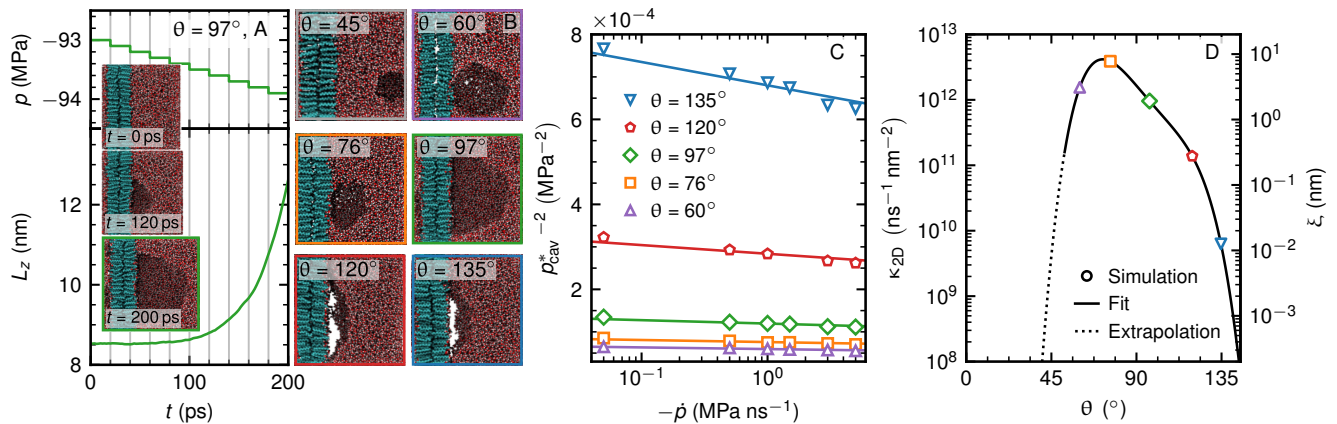


Figure 3. (A) Time-dependent pressure ( $p$ , top) and simulation box size ( $L_z$ , bottom) during a pressure ramp simulation with a pressure rate of  $\dot{p} = -5$  MPa/ns for a system with a surface contact angle of  $\theta = 97^\circ$ . The presented trajectory corresponds to the final 200 ps prior to cavitation, identified as a 50% increase of  $L_z$  relative to its initial value  $L_z^0 = 8$  nm. We find a cavitation pressure of  $p_{\text{cav}}^* = -93.9$  MPa. Vertical lines mark individual simulation segments at constant pressure. The inset shows consecutive snapshots of the cavitation event. (B) Cavitation configurations with  $L_z/L_z^0 = 3/2$  for different contact angles. We also present trajectory visualizations for  $\theta = 45^\circ$  (upper left panel) (multimedia available online) and  $\theta = 135^\circ$  (lower right panel) (multimedia available online). (C) Simulation results for  $1/p_{\text{cav}}^{*2}$  versus  $\dot{p}$  for different contact angles. The lines are fits of Eq. 1 to the data, where  $\kappa_{2D}$  is the only fitting parameter. (D) Results for  $\kappa_{2D}$  (left scale) and the ratio  $\xi = \kappa_{2D}/\kappa_{3D}$  (right scale) as a function of contact angle  $\theta$ . The solid black line is a fit of Eq. S13 in the Supplementary Material, section S3. For  $\theta < 52^\circ$ , the fit does not serve as a reliable extrapolation and is denoted as a broken line.

Instead, we apply negative pressures that decrease linearly over time as  $p(t) = \dot{p}t$  with different fixed pressure ramp rates  $\dot{p} < 0$ , as used before for bulk cavitation<sup>36</sup> and described in the methods section.

Fig. 3 summarizes our simulation results. Panel A illustrates a cavitation event on a hydrophobic surface with contact angle  $\theta = 97^\circ$ , where a vapor bubble forms at the surface (see inset snapshots) due to the progressively decreasing pressure over time (upper graph). The simulation trajectory consists of a sequence of 20-ps-long simulations (delineated by gray vertical lines), each at a constant applied pressure that decreases in discrete steps of 0.1 MPa, which corresponds to a mean pressure rate of  $\dot{p} = -5$  MPa/ns. The formation of the bubble is monitored by the box size normal to the surface  $L_z$  (bottom graph). We define cavitation to take place when the box size  $L_z$  increases by 50% compared to its initial value  $L_z^0$ , which in this specific example yields a cavitation pressure  $p_{2D\text{cav}}^* = -93.9$  MPa. It is important to note that the cavitation pressure in the pressure-ramp ensemble  $p_{2D\text{cav}}^*$  is different from the cavitation pressure  $p_{2D\text{cav}}$  in the constant-pressure ensemble given in Eq. 12, which normal pressure will be determined later.

Representative snapshots of cavitation for  $L_z/L_z^0 = 3/2$  at surfaces with different contact angles are presented in Fig. 3B. We also provide trajectory visualizations for  $\theta = 45^\circ$  (upper left panel) (multimedia available online) and  $\theta = 135^\circ$  (lower right panel) (multimedia available online). Fig. 3C shows  $1/p_{\text{cav}}^{*2}$  versus the negative pressure-ramp rate  $-\dot{p}$ . Each data point represents an average over 10 independent simulations. The solid lines

are fits of the kinetic theory (Eq. 1 and using  $G^* = G_{2D}^*$ ), assuming pure surface cavitation which yield the value of  $\kappa_{2D}(\theta)$  for each  $\theta$ . For the lowest contact angle of  $45^\circ$ , bubble cavitation occurs in the bulk. Therefore, this surface is not included in the analysis in Fig. 3C. The resulting values for  $\kappa_{2D}$  (symbols) are shown as a function of the surface contact angle  $\theta$  in Fig. 3D. We also denote the characteristic length  $\xi = \kappa_{2D}/\kappa_{3D}$  by the scale on the right, which represents the water slab height for which the surface cavitation attempt frequency  $\kappa_{2D}$  equals the bulk attempt frequency  $\kappa_{3D}$ . It can be seen that  $\xi$  exhibits a maximum around  $\theta \approx 75^\circ$  and goes dramatically down with increasing contact angle from approximately 10 to  $10^{-2}$  nm. This suggests that a hydrophilic surface produces more cavitation nuclei in a given time than a hydrophobic surface, which is interesting since it contrasts with the pronounced density fluctuations at hydrophobic surfaces<sup>57</sup> (alternatively, it could reflect inaccuracies of the bulk and surface-barrier-free energy expressions). Clearly, this variation of  $\kappa_{2D}$  is subdominant compared to the variation of the exponential barrier energy in Eq. 11, but nevertheless has to be included for a quantitative comparison of surface and bulk cavitation kinetics. For our subsequent analyses, we fit our simulation data for the logarithm of  $\kappa_{2D}$  in Fig. 3D to a polynomial shown as a solid line, as detailed in the Supplementary Material, section S3. While polynomial fits are suitable for interpolation, they are less reliable for extrapolation. We therefore trust the polynomial fit only down to a constant angle extrapolation interval  $60^\circ - \theta^* = 8^\circ$  which is half the angle distance between the two lower data points



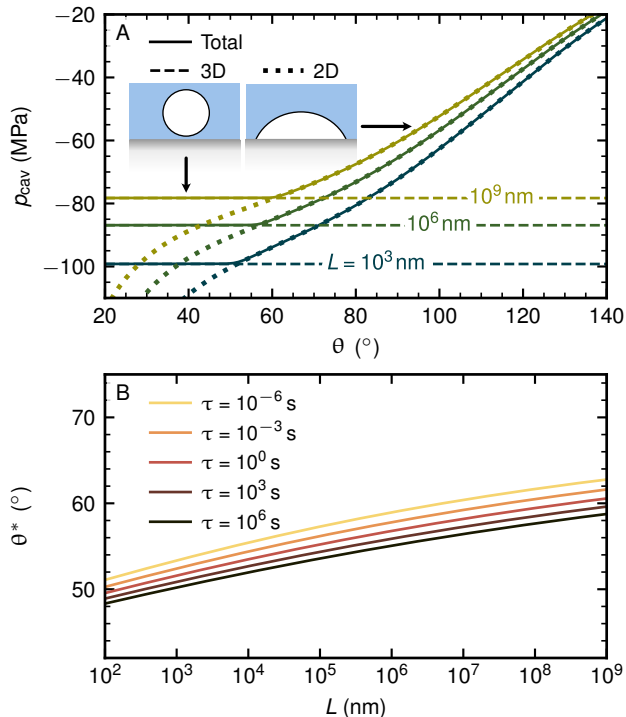


Figure 4. (A) Cavitation pressure  $p_{\text{cav}}$  of a water-filled cubic container as a function of the contact angle  $\theta$  of the defect-free inner walls, for a fixed waiting time of  $\tau = 1$  s, computed by numerically inverting Eq. 3 for  $N_{\text{def}} = 0$  (solid lines). Different colors represent different cube sizes  $L$ . Dotted lines show the 2D cavitation pressure according to Eq. 12, while dashed horizontal lines denote the 3D cavitation pressure based on Eq. 7. (B) Crossover contact angle  $\theta^*$ , where  $k_{2\text{D}} = k_{3\text{D}}$ , as a function of container size  $L$  for different waiting times  $\tau$ , according to Eq. 13.

$76^\circ - 60^\circ = 16^\circ$ . Therefore the fit for  $\theta < \theta^* = 52^\circ$  is shown as a broken line.

#### D. Kinetic competition between cavitation in bulk and at a defect-free surface

In the absence of defects, we set  $N_{\text{def}} = 0$  in Eq. 3. The cavitation pressure  $p_{\text{cav}}$  cannot be derived analytically, therefore, we solve Eq. 3 numerically and plot  $p_{\text{cav}}$  in Fig. 4 A (solid lines) against the surface contact angle  $\theta$  for different cube sizes  $L$  and a fixed waiting time of  $\tau = k_{\text{tot}}^{-1} = 1$  s. For hydrophilic surfaces with small  $\theta$ ,  $p_{\text{cav}}$  is dominated by bulk cavitation (thus,  $k_{\text{tot}} \approx k_{3\text{D}}$ ) and becomes independent of  $\theta$ , as described by Eq. 7 and represented by the horizontal dashed lines. For larger contact angles  $\theta$ , the cavitation pressure is well described by the surface prediction (Eq. 12), shown as dotted lines, which indicates that cavitation for large  $\theta$  predominantly occurs at surfaces.

It is seen that cavitation shifts from the bulk (3D) to

the surface (2D) pathway rather abruptly at a distinct crossover contact angle  $\theta^*$ , which marks the onset of surface cavitation. Thus,  $\theta^*$  is identified as the intersection of the bulk prediction (dashed lines) and the surface prediction (dotted lines) in Fig. 4 A. In Supplementary Material, section S4, we present results for a range of different waiting times  $\tau$  from  $10^{-3}$  to  $10^3$  s, showing the same sharp transition between the surface-dominated and the bulk-dominated regimes. By equating Eq. 7 and Eq. 12, we obtain an exact expression for the critical system size  $L^*$  at which the transition takes place

$$L^* = \left[ 6\tau\kappa_{2\text{D}}(\theta)(\kappa_{3\text{D}}\tau)^{-h(\theta)} \right]^{1/[3h(\theta)-2]}, \quad (13)$$

whose inverse (i.e.,  $\theta^*$  as a function of  $L$ ) is presented in Fig. 4 B for various cavitation times  $\tau$ . It transpires that  $\theta^*$  varies within a narrow window between  $50^\circ$  and  $60^\circ$  for order-of-magnitude variations of system size  $L$  and cavitation time  $\tau$ .

This weak dependence of  $\theta^*$  on  $L$  and  $\tau$  can be understood from the analytical inverse of Eq. 13 valid for small  $\theta$ ,

$$\theta^* \approx \left\{ \frac{16 \ln[L/(6\xi)]}{3 \ln(\kappa_{3\text{D}}L^3\tau)} \right\}^{1/4}, \quad (14)$$

see Supplementary Material, section S5 for the derivation. The critical contact angle depends as a fourth root on the logarithm of  $L$  and  $\tau$ , which is an extremely weakly varying function.

We conclude that surface cavitation occurs if the contact angle of the confining surfaces exceeds the threshold value  $\theta^*$ , which is largely independent of system size and waiting time. Although surfaces with contact angles below the threshold (i.e., for  $\theta < \theta^*$ ) do have a lower cavitation free energy barrier compared to bulk cavitation, as predicted by Eq. 9, they exhibit a smaller cavitation rate due to the different attempt frequencies at a surface and in bulk, as quantified by the length scale  $\xi$ . This renders surface cavitation on hydrophilic surfaces less likely than bulk cavitation.

#### E. Cavitation at surface defects

Real-world surfaces are rich in surface defects such as vacancies, disordered regions, variations in material composition and adsorbed organic or inorganic species<sup>58</sup>. We model defects as circular patches with radius  $R_{\text{def}}$  and contact angle  $\theta_{\text{def}}$ , as illustrated in Fig. 5 A. We assume the defects to be larger than the critical bubble base radius  $a^*$  and much smaller than the system size  $L$ ,  $a^* \ll R_{\text{def}} \ll L$ . With these assumptions, the single defect cavitation rate in Eq. 3 is given in analogy to Eq. 11 as

$$k_{\text{def}} = \kappa_{2\text{D}}(\theta_{\text{def}})A_{\text{def}} e^{-\beta G_{2\text{D}}^*(\theta_{\text{def}})}, \quad (15)$$

with the defect surface area given by  $A_{\text{def}} = \pi R_{\text{def}}^2$  and the attempt frequency density  $\kappa_{2\text{D}}$  and the free energy barrier  $G_{2\text{D}}^*$  determined by the defect contact angle  $\theta_{\text{def}}$ . The defect cavitation pressure follows from  $\tau^{-1} = N_{\text{def}} k_{\text{def}}$  by using Eq. 15 and Eq. 9 as

$$p_{\text{defcav}}^2 = \frac{16\pi\gamma^3}{3k_{\text{B}}T} \frac{h(\theta_{\text{def}})}{\ln[\kappa_{2\text{D}}(\theta_{\text{def}})\pi R_{\text{def}}^2 \tau N_{\text{def}}]}. \quad (16)$$

The total cavitation rate in Eq. 3 describes the kinetic competition between cavitation in bulk, at surfaces and at defects. The cavitation pressure resulting from this competition is determined by solving Eq. 3 in conjunction with Eqs. 6, 11, 15 for a given set of parameters  $L$ ,  $\tau$ ,  $\theta$ ,  $N_{\text{def}}$ ,  $\theta_{\text{def}}$  and  $R_{\text{def}}$ .

For the following discussion, we assume that the surface is sufficiently hydrophilic so that  $k_{2\text{D}} \ll k_{3\text{D}}$  and cavitation at the defect-free surface parts can be neglected. The solid lines in Fig. 5B show the cavitation pressure in a 1 mL cube of water ( $L = 1$  cm) in the presence of a single surface defect,  $N_{\text{def}} = 1$ , as a function of the defect radius  $R_{\text{def}}$  for different defect contact angles  $\theta_{\text{def}}$ . For a given  $\theta_{\text{def}}$ , a well-defined crossover radius  $R_{\text{def}}^*$  emerges at which the system transitions from bulk cavitation for small  $R_{\text{def}}$ , where the bulk prediction Eq. 7 (dashed line) is valid, to defect cavitation for large  $R_{\text{def}}$ , where the prediction in Eq. 16 (dotted lines) is valid. The crossover radius  $R_{\text{def}}^*$  grows as  $\theta_{\text{def}}$  approaches  $\theta^*$  from above. Conversely, for increasing  $\theta_{\text{def}}$  the crossover radius  $R_{\text{def}}^*$  approaches sub-nanometer values (where our continuum model will eventually break down). The results in Fig. 5B show that cavitation is dominated by defects with a radius larger than a critical value  $R_{\text{def}}^*$  and occurs at a rate  $N_{\text{def}} k_{\text{def}}$ ; even a single hydrophobic defect can dominate the cavitation kinetics in macroscopic systems.

The crossover radius  $R_{\text{def}}^*$  between the cavitation pressures for the bulk and defect pathways follows from equating Eqs. 7 and 16 as

$$R_{\text{def}}^{*2} = \frac{(\kappa_{3\text{D}} L^3 \tau)^{h(\theta_{\text{def}})}}{\pi \kappa_{2\text{D}}(\theta_{\text{def}}) \tau N_{\text{def}}}. \quad (17)$$

In Fig. 5C we show  $R_{\text{def}}^*$  as a function of system size  $L$  for a waiting time of  $\tau = 1$  s and a single defect ( $N_{\text{def}} = 1$ ) for four different defect contact angles. As the system size increases, a larger defect is required to induce defect cavitation. Conversely, for larger defect contact angle  $\theta_{\text{def}}$ , the crossover radius  $R_{\text{def}}^*$  decreases and reaches the nanometer scale even for macroscopically large systems. For a surface with multiple defects,  $N_{\text{def}} > 1$ , the required defect radius  $R_{\text{def}}^*$  is expected to decrease proportionally to  $\sim N_{\text{def}}^{-1/2}$ , as predicted by Eq. 17.

Finally, we check our theoretical predictions by explicit simulations of a system featuring one defect. We choose a mildly hydrophobic surface with a contact angle of  $\theta = 97^\circ$  on which we create one circular defect by removing surface molecules within a radius of  $R_{\text{def}}$  on one monolayer, thereby forming a hydrophobic pit with

a depth of 1 nm. Water does not enter the pit because of its hydrophobic interior, creating a vapor bubble, corresponding to a defect contact angle of  $\theta_{\text{def}} \approx 180^\circ$ . To avoid cavitation at the opposite monolayer, we make it hydrophilic with a contact angle of  $42^\circ$ . Using the pressure ramp protocol, we consistently observe bubble formation at the hydrophobic pit, as shown in the snapshots in Fig. 5D, despite the rest of the surface being mildly hydrophobic. Trajectory visualizations for  $R_{\text{def}} = 1$  nm (upper panel) (multimedia available online) and  $R_{\text{def}} = 2$  nm (lower panel) (multimedia available online) defects are provided as well. Using a pressure rate of  $\dot{p} = -5$  MPa/ns, a defect-free surface induces surface cavitation at  $p_{\text{cav}}^* = -95 \pm 1$  MPa, as seen in Fig. 3C. In contrast, the systems with surface defects of 1 and 2 nm radii cavitate already at  $p_{\text{cav}}^* = -66$  and  $-45 \pm 2$  MPa, respectively. These results qualitatively agree with our predictions in Fig. 5B that even nanometer-sized surface defects can act as cavitation nuclei. The influence of defects on cavitation is studied in more detail in our follow-up study<sup>59</sup>.

#### IV. CONCLUSION

By combining MD simulations with the CNT framework, we explore the kinetic competition among the three fundamental pathways of cavitation in water under negative pressure: bulk cavitation, surface cavitation and defect-induced cavitation. For defect-free surfaces, the prevalent cavitation pathway shifts abruptly from bulk to surfaces when the surface contact angle increases above a threshold of  $\theta^* \approx 50^\circ$  to  $60^\circ$ , depending slightly on system size and waiting time. The typical cavitation pressure decreases in magnitude from about  $p_{\text{cav}} \approx -100$  MPa for bulk to about  $p_{\text{cav}} \approx -30$  MPa for hydrophobic surface cavitation. Even the presence of a single nanoscopic hydrophobic surface defect dominates the cavitation kinetics and substantially raises the cavitation pressure, depending on the defect contact angle and defect size. Since even with the most advanced fabrication techniques surface defects are unavoidable and experimental cavitation pressures for typical surface materials are far above the predicted value for bulk cavitation and low cavitation pressures around  $p_{\text{cav}} \approx -100$  MPa are only achieved in micro-sized defect-free quartz cavities<sup>16-18</sup>.

While hydrophobic aggregates reduce the water stability against cavitation, individual dispersed molecules generally have a minimal effect<sup>35,36</sup>. Viscosifying agents, such as polymers, slow down cavitation kinetics, by influencing the prefactor  $\kappa$  in Eqs. (6) and (11) without altering the exponential term. However, surfaces with contact angles exceeding the ‘‘Berg limit’’ of approximately  $65^\circ$ —coincidentally near the crossover contact angle—are prone to adhesion of amphiphilic molecules<sup>60-63</sup>. This adhesion can render such surfaces more hydrophilic and coat surface defects<sup>62</sup>, thereby suppressing surface cavi-

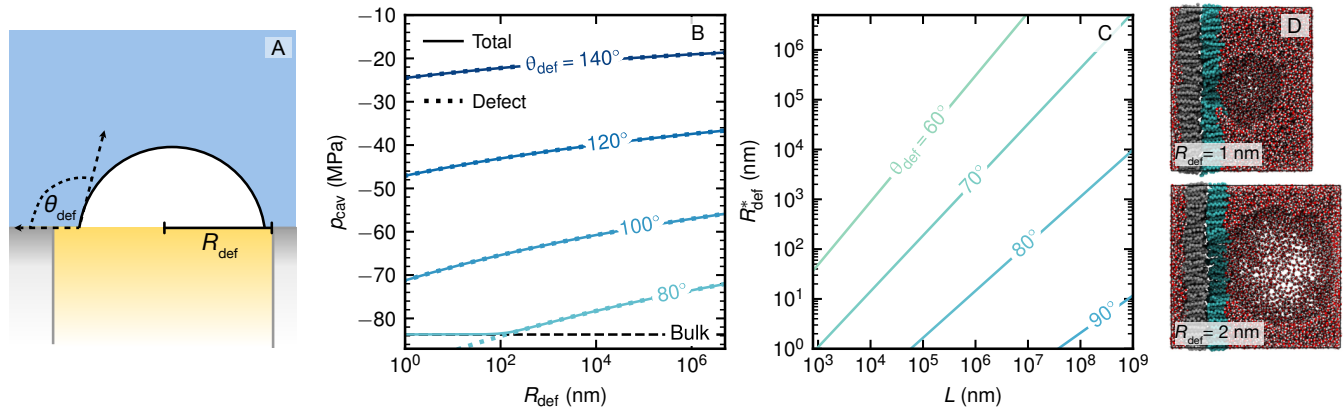


Figure 5. (A) Illustration of a cavitation bubble on a circular surface defect with radius  $R_{\text{def}}$  and contact angle  $\theta_{\text{def}}$  on a flat surface of contact angle  $\theta$ . (B) Cavitation pressure of a water-filled container with a single surface defect  $N_{\text{def}} = 1$  as a function of  $R_{\text{def}}$  for different  $\theta_{\text{def}}$ . Solid lines are obtained by numerically solving Eq. 3 for a waiting time of  $\tau = 1$  s and a container size of  $L = 1$  cm (volume of 1 mL). Dotted lines show the limiting pressure for a large defect, given by Eq. 16, whereas the horizontal dashed line shows the bulk cavitation pressure Eq. 7. (C) Crossover defect radius  $R_{\text{def}}^*$  as a function of container size  $L$  for a fixed waiting time of  $\tau = 1$  s from Eq. 17. (D) Simulation snapshots for box expansions of  $L_z/L_z^0 = 3/2$  after cavitation in systems with a surface contact angle of  $97^\circ$  and cylindrical hydrophobic pits, from pressure-ramp simulations at a rate of  $\dot{p} = -5$  MPa/ns. The pits have radii of  $R_{\text{def}} \approx 1$  nm (upper panel) (multimedia available online) and 2 nm (lower panel) (multimedia available online).

tation. This mechanism might explain the prevention of embolisms through lipid adsorption in tree sap<sup>64</sup> or the increased cavitation stability observed when amphiphilic polymers are added to water<sup>65,66</sup>. Exploring the effect of molecular adsorption on defects and cavitation is an intriguing question, which we aim to pursue in upcoming studies.

In this study, we focused on pressure-induced cavitation in water at constant temperature. However, the methods developed here can be extended to other liquids and applied to cavitation in superheated liquids or nucleation in supersaturated solutions. In such systems, surface and defect nucleation are expected to play similarly critical roles.

## V. SUPPLEMENTARY MATERIAL

The supplementary material contains additional information on fitting the kinetic prefactor, the cavitation pressure for various waiting times  $\tau$ , the relation between surface polarity  $\alpha$  and contact angle of the SAM surface.

## ACKNOWLEDGMENTS

M.K. acknowledges financial support from the Slovenian Research and Innovation Agency ARIS (contracts P1-0055 and J1-4382).

## DATA AVAILABILITY STATEMENT

All simulation input files as well as Python functions to fit  $\kappa_{2D}$  and perform further analysis from the simulations are available on Zenodo.

## REFERENCES

- <sup>1</sup>A. J. Coleman and J. E. Saunders, “A survey of the acoustic output of commercial extracorporeal shock wave lithotripters,” *Ultrasound Med Biol* **15**, 213–227 (1989).
- <sup>2</sup>F. Caupin and E. Herbert, “Cavitation in water: a review,” *Comptes Rendus Physique* **7**, 1000–1017 (2006).
- <sup>3</sup>A. Fall, J. D. Rimstidt, and R. J. Bodnar, “The effect of fluid inclusion size on determination of homogenization temperature and density of liquid-rich aqueous inclusions,” *American Mineralogist* **94**, 1569–1579 (2009).
- <sup>4</sup>M. Dular, B. Bachert, B. Stoffel, and B. Širok, “Relationship between cavitation structures and cavitation damage,” *Wear* **257**, 1176–1184 (2004).
- <sup>5</sup>F. Reuter, C. Deiter, and C.-D. Ohl, “Cavitation erosion by shockwave self-focusing of a single bubble,” *Ultrason Sonochem* **90**, 106131 (2022).
- <sup>6</sup>U. Adhikari, A. Goliaei, and M. L. Berkowitz, “Mechanism of membrane poration by shock wave induced nanobubble collapse: A molecular dynamics study,” *J. Phys. Chem. B* **119**, 6225–6234 (2015).
- <sup>7</sup>D. Custodio, C. Henocho, and H. Johari, “Cavitation on hydrofoils with leading edge protuberances,” *Ocean Engineering* **162**, 196–208 (2018).
- <sup>8</sup>X. Noblin, N. Rojas, J. Westbrook, C. Llorens, M. Argentina, and J. Dumais, “The fern sporangium: a unique catapult,” *Science* **335**, 1322–1322 (2012).
- <sup>9</sup>M. Verslius, B. Schmitz, A. von der Heydt, and D. Lohse, “How snapping shrimp snap: Through cavitating bubbles,” *Science* **289**, 2114 (2000).



- <sup>10</sup>A. M. Smith, “Negative pressure generated by octopus suckers: a study of the tensile strength of water in nature,” *J. Exp. Biol.* **157**, 257–271 (1991).
- <sup>11</sup>P. G. Debenedetti, *Metastable Liquids: Concepts and Principles*, Vol. 1 (Princeton University Press, 1996).
- <sup>12</sup>J. C. Fisher, “The Fracture of Liquids,” *Journal of Applied Physics* **19**, 1062–1067 (1948).
- <sup>13</sup>F. Caupin, “Liquid-vapor interface, cavitation, and the phase diagram of water,” *Phys. Rev. E* **71**, 051605 (2005).
- <sup>14</sup>F. Caupin and A. D. Stroock, “The stability limit and other open questions on water at negative pressure,” *Liquid Polymorphism* **152**, 51–80 (2013).
- <sup>15</sup>M. E. M. Azouzi, C. Ramboz, J.-F. Lenain, and F. Caupin, “A coherent picture of water at extreme negative pressure,” *Nat. Phys.* **9**, 38–41 (2013).
- <sup>16</sup>Q. Zheng, D. J. Durben, G. H. Wolf, and C. A. Angell, “Liquids at large negative pressures: Water at the homogeneous nucleation limit,” *Science* **254**, 829–832 (1991), <https://www.science.org/doi/pdf/10.1126/science.254.5033.829>.
- <sup>17</sup>A. Alvarenga, M. Grimsditch, and R. Bodnar, “Elastic properties of water under negative pressures,” *J. Chem. Phys.* **98**, 8392–8396 (1993).
- <sup>18</sup>M. E. M. Azouzi, C. Ramboz, J.-F. Lenain, and F. Caupin, “A coherent picture of water at extreme negative pressure,” *Nature Phys* **9**, 38–41 (2013).
- <sup>19</sup>F. Caupin, “Escaping the no man’s land: Recent experiments on metastable liquid water,” *J. Non-Cryst. Solids* **407**, 441–448 (2015).
- <sup>20</sup>S. F. Jones, G. M. Evans, and K. P. Galvin, “Bubble nucleation from gas cavities — a review,” *Advances in Colloid and Interface Science* **80**, 27–50 (1999).
- <sup>21</sup>H. B. Marschall, K. A. Mørch, A. P. Keller, and M. Kjeldsen, “Cavitation inception by almost spherical solid particles in water,” *Physics of Fluids* **15**, 545–553 (2003).
- <sup>22</sup>R. P. Sear, “Nucleation: theory and applications to protein solutions and colloidal suspensions,” *J. Condens. Matter Phys.* **19**, 033101 (2007).
- <sup>23</sup>K. A. Mørch, “Reflections on cavitation nuclei in water,” *Phys. Fluids* **19** (2007).
- <sup>24</sup>S.-i. Tsuda, S. Takagi, and Y. Matsumoto, “A study on the growth of cavitation bubble nuclei using large-scale molecular dynamics simulations,” *Fluid Dyn. Res.* **40**, 606 (2008).
- <sup>25</sup>T. Groß and P. Pelz, “Diffusion-driven nucleation from surface nuclei in hydrodynamic cavitation,” *J. Fluid Mech.* **830**, 138–164 (2017).
- <sup>26</sup>Z. Gao, W. Wu, and B. Wang, “The effects of nanoscale nuclei on cavitation,” *J. Fluid Mech.* **911**, A20 (2021).
- <sup>27</sup>E. N. Harvey, D. K. Barnes, W. D. McElroy, A. H. Whiteley, D. C. Pease, and K. W. Cooper, “Bubble formation in animals. I. Physical factors,” *Journal of Cellular and Comparative Physiology* **24**, 1–22 (1944).
- <sup>28</sup>A. A. Atchley and A. Prosperetti, “The crevice model of bubble nucleation,” *The Journal of the Acoustical Society of America* **86**, 1065–1084 (1989).
- <sup>29</sup>B. M. Borkent, S. Gekle, A. Prosperetti, and D. Lohse, “Nucleation threshold and deactivation mechanisms of nanoscopic cavitation nuclei,” *Phys. Fluids* **21** (2009).
- <sup>30</sup>P. Pfeiffer, M. Shahrooz, M. Tortora, C. M. Casciola, R. Holman, R. Salomir, S. Meloni, and C.-D. Ohl, “Heterogeneous cavitation from atomically smooth liquid–liquid interfaces,” *Nat. Phys* **18**, 1431–1435 (2022).
- <sup>31</sup>G. Menzl, M. A. Gonzalez, P. Geiger, F. Caupin, J. L. F. Abascal, C. Valeriani, and C. Dellago, “Molecular mechanism for cavitation in water under tension,” *Proceedings of the National Academy of Sciences* **113**, 13582–13587 (2016).
- <sup>32</sup>C. P. Lamas, C. Vega, E. G. Noya, and E. Sanz, “The water cavitation line as predicted by the tip4p/2005 model,” *J. Chem. Phys.* **158** (2023).
- <sup>33</sup>S. H. Min and M. L. Berkowitz, “Bubbles in water under stretch-induced cavitation,” *J. Chem. Phys.* **150** (2019).
- <sup>34</sup>H. Xie, Y. Xu, and C. Zhong, “A study of cavitation nucleation in pure water using molecular dynamics simulation,” *Chin. Phys. B* **31**, 114701 (2022).
- <sup>35</sup>Y. Zhou, B. Li, Y. Gu, and M. Chen, “A molecular dynamics simulation study on the cavitation inception of water with dissolved gases,” *Mol. Phys.* **117**, 1894–1902 (2019).
- <sup>36</sup>M. Kanduč, E. Schneck, P. Loche, S. Jansen, H. J. Schenk, and R. R. Netz, “Cavitation in lipid bilayers poses strict negative pressure stability limit in biological liquids,” *PNAS* **117**, 10733–10739 (2020).
- <sup>37</sup>D. Dockar, M. K. Borg, and J. M. Reese, “Mechanical Stability of Surface Nanobubbles,” *Langmuir* **35**, 9325–9333 (2019).
- <sup>38</sup>M. Šako, R. R. Netz, and M. Kanduč, “Impact of nanoscopic impurity aggregates on cavitation in water,” under review **xx** (2024).
- <sup>39</sup>B. Li, Y. Gu, and M. Chen, “Cavitation inception of water with solid nanoparticles: A molecular dynamics study,” *Ultrason. Sonochem.* **51**, 120–128 (2019).
- <sup>40</sup>M. Kanduč, E. Schneck, and R. R. Netz, “Attraction between hydrated hydrophilic surfaces,” *Chem. Phys. Lett.* **610**, 375–380 (2014).
- <sup>41</sup>M. Kanduč and R. R. Netz, “Atomistic simulations of wetting properties and water films on hydrophilic surfaces,” *The Journal of Chemical Physics* **146**, 164705 (2017).
- <sup>42</sup>C. Oostenbrink, A. Villa, A. E. Mark, and W. F. V. Gunsteren, “A biomolecular force field based on the free enthalpy of hydration and solvation: The GROMOS force-field parameter sets 53A5 and 53A6,” *Journal of Computational Chemistry* **25**, 1656–1676 (2004).
- <sup>43</sup>H. J. C. Berendsen, J. R. Grigera, and T. P. Straatsma, “The missing term in effective pair potentials,” *J. Phys. Chem.* **91**, 6269–6271 (1987).
- <sup>44</sup>M. J. Abraham, T. Murtola, R. Schulz, S. Páll, J. C. Smith, B. Hess, and E. Lindahl, “GROMACS: High performance molecular simulations through multi-level parallelism from laptops to supercomputers,” *SoftwareX* **1–2**, 19–25 (2015).
- <sup>45</sup>G. Bussi, D. Donadio, and M. Parrinello, “Canonical sampling through velocity rescaling,” *The Journal of Chemical Physics* **126**, 014101 (2007).
- <sup>46</sup>G. Menzl and C. Dellago, “Effect of entropy on the nucleation of cavitation bubbles in water under tension,” *J. Chem. Phys.* **145**, 211918 (2016).
- <sup>47</sup>P. Hänggi, P. Talkner, and M. Borkovec, “Reaction-rate theory: fifty years after kramers,” *Rev. Mod. Phys.* **62**, 251 (1990).
- <sup>48</sup>J. Kubelka, J. Hofrichter, and W. A. Eaton, “The protein folding ‘speed limit’,” *Curr. Opin. Struct. Biol.* **14**, 76 (2004).
- <sup>49</sup>S. Acharya and B. Bagchi, “Rate theory of gas–liquid nucleation: Quest for the elusive quantitative accuracy,” *J. Chem. Phys.* **160**, 174503 (2024).
- <sup>50</sup>E. Herbert, S. Balibar, and F. Caupin, “Cavitation pressure in water,” *Physical Review E* **74**, 041603 (2006).
- <sup>51</sup>M. Blander and J. L. Katz, “Bubble nucleation in liquids,” *AIChE J.* **21**, 833–848 (1975).
- <sup>52</sup>M. Pettersen, S. Balibar, and H. Maris, “Experimental investigation of cavitation in superfluid he 4,” *Phys. Rev. B* **49**, 12062 (1994).
- <sup>53</sup>W. J. Galloway, “An experimental study of acoustically induced cavitation in liquids,” *J. Acoust. Soc. Am.* **26**, 849–857 (1954).
- <sup>54</sup>R. E. Apfel and M. P. Smith, “The tensile strength of di-ethyl ether using briggs’s method,” *J. Appl. Phys.* **48**, 2077–2078 (1977).
- <sup>55</sup>Y. Ohde, H. Watanabe, K. Motoshita, Y. Tanzawa, *et al.*, “Raising of negative pressure to around-200 bar for some organic liquids in a metal berthelot tube,” *J. Phys. D Appl. Phys.* **26**, 1188 (1993).
- <sup>56</sup>V. E. Vinogradov and P. A. Pavlov, “The boundary of limiting superheats of n-heptane, ethanol, benzene, and toluene in the region of negative pressures,” *High Temp.* **38**, 379–383 (2000).
- <sup>57</sup>N. B. Rego and A. J. Patel, “Understanding hydrophobic effects: Insights from water density fluctuations,” *Annu. Rev. Condens.*

- Matter Phys. **13**, 303 (2022).
- <sup>58</sup>I. Siretanu, D. van den Ende, and F. Mugele, “Atomic structure and surface defects at mineral-water interfaces probed by in situ atomic force microscopy,” *Nanoscale* **8**, 8220–8227 (2016).
- <sup>59</sup>M. Šako, F. Staniscia, R. Netz, E. Schneck, and M. Kanduč, “Effect of surface defects on heterogeneous cavitation in water,” *arxiv* **xx** (2024).
- <sup>60</sup>E. A. Vogler, “Structure and reactivity of water at biomaterial surfaces,” *Adv. Colloid Interface Sci.* **74**, 69–117 (1998).
- <sup>61</sup>A. Rosenhahn, S. Schilp, H. J. Kreuzer, and M. Grunze, “The role of “inert” surface chemistry in marine biofouling prevention,” *Phys. Chem. Chem. Phys.* **12**, 4275–4286 (2010).
- <sup>62</sup>M. Šako, F. Staniscia, E. Schneck, R. R. Netz, and M. Kanduč, “Conditions for the stable adsorption of lipid monolayers to solid surfaces,” *PNAS Nexus* **2**, pgad190 (2023).
- <sup>63</sup>M. Kanduč, E. Schneck, and R. R. Netz, “Understanding the “berg limit”: the 65° contact angle as the universal adhesion threshold of biomatter,” *Phys. Chem. Chem. Phys.* **26**, 713–723 (2024).
- <sup>64</sup>H. J. Schenk, K. Steppe, and S. Jansen, “Nanobubbles: a new paradigm for air-seeding in xylem,” *Trends Plant Sci.* **20**, 199–205 (2015).
- <sup>65</sup>E. A. Brujan, A. F. H. Al-Hussany, R. L. Williams, and P. R. Williams, “Cavitation erosion in polymer aqueous solutions,” *Wear* **264**, 1035–1042 (2008).
- <sup>66</sup>A. A. Gruzdkov and Yu. V. Petrov, “Cavitation breakup of low- and high-viscosity liquids,” *Tech. Phys.* **53**, 291–295 (2008).

# Water cavitation results from the kinetic competition of bulk, surface and surface-defect nucleation events: Supplementary Material

Philip Loche,<sup>1,2</sup> Matej Kanduč,<sup>3</sup> Emanuel Schneck,<sup>4</sup> and Roland R. Netz\*

<sup>1</sup>Laboratory of Computational Science and Modeling, IMX,

École Polytechnique Fédérale de Lausanne, 1015 Lausanne, Switzerland

<sup>2</sup>Fachbereich Physik, Freie Universität Berlin, 14195 Berlin, Germany

<sup>3</sup>Department of Theoretical Physics, Jožef Stefan Institute, 1000 Ljubljana, Slovenia

<sup>4</sup>Physics Department, Technische Universität Darmstadt, 64289 Darmstadt, Germany

## CONTENTS

S1. Relation between surface polarity $\alpha$ and contact angle $\theta$	S1
S2. Fitting the kinetic prefactor	S2
S3. Fitting $\kappa_{2D}(\theta)$	S3
S4. Cavitation pressure for various waiting times $\tau$	S3
S5. Analytic estimate for the crossover contact angle $\theta^*$	S3
References	S4

### S1. RELATION BETWEEN SURFACE POLARITY $\alpha$ AND CONTACT ANGLE $\theta$

The used model surface, resembling SAMs with tunable partial charges in the hydroxyl groups, has been thoroughly studied elsewhere.<sup>1</sup> Fig. S1 shows the cosine of the contact angle  $\cos \theta$  as a function of the scaling factor  $\alpha$  of the hydroxyl group's partial charges. For  $\alpha = 0$  (i.e., the partial charges of the hydroxyl groups are 0), the surface is nonpolar, resulting in a contact angle of  $135^\circ$ . For  $\alpha > 0.86$ , the surface exhibit complete wetting, with  $\theta = 0$ . We fit the simulation data to

$$\cos \theta = c_0 + c_1 \alpha + c_2 \alpha^2 + c_3 \alpha^3, \quad (\text{S1})$$

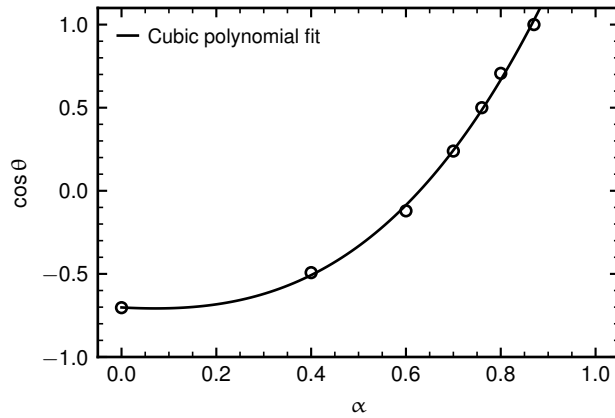


Figure S1. Cosine of the contact angle  $\theta$  as a function of the SAM's surface polarity  $\alpha$ . Data is taken from Ref. 1. The solid line is the fit of Eq. S1 to the data points.

\* rnetz@physik.fu-berlin.de

yielding the coefficients:  $c_0 = -0.70$ ,  $c_1 = -0.09$ ,  $c_2 = 0.65$ , and  $c_3 = 1.99$ . The fit is shown as a solid line in Fig. S1. This fit was used to determine the partial charges corresponding to a contact angle of  $\theta = 60^\circ$ , which had not been previously determined.

## S2. FITTING THE KINETIC PREFACTOR

Using classical nucleation theory, one can derive the free energy barriers as given by Eqs. 3 and 7. However, the kinetic prefactor is governed by hydrodynamic and dissipation effects, making it difficult to assess analytically. Atomistic simulations provide a way to extract this factor. A straightforward approach might be to simulate a system at a constant negative pressure and track bubble formation. Unfortunately, this approach makes it challenging to observe cavity formation within practical simulation times, particularly without prior knowledge on the cavitation pressure. Therefore, we apply a time-dependent pressure ramp in the form

$$p(t) = \dot{p} t, \quad (\text{S2})$$

to sample these rare events by solving time-dependent rate equations. Under this time-dependent pressure, the cavitation rate also becomes time-dependent and can be, in the Kramers framework, approximately expressed as

$$k(t) = k_0 e^{-\beta G^*(t)}. \quad (\text{S3})$$

Note that for clarity we leave out the subscripts 3D or 2D since the equations are valid for both. The probability  $f(t)$  that the system has not yet crossed the barrier obeys a first-order rate equation

$$\dot{f}(t) = -k(t) f(t), \quad (\text{S4})$$

with the formal solution

$$f(t) = e^{-k_0 I(t)}, \quad (\text{S5})$$

where  $I(t)$  is given by

$$I(t) = \int_0^t e^{-\beta G^*(t')} dt'. \quad (\text{S6})$$

In our pressure-ramp simulations, the free-energy barrier (given by Eqs. 3 or 7) decreases inversely with the square of time as

$$\beta \Delta G^*(t) = \left( \frac{\zeta}{t} \right)^2, \quad (\text{S7})$$

with the time constants of the barrier  $\zeta$  for homogeneous (3D) and heterogeneous (2D) cavitation given by

$$(\zeta_{3\text{D}})^2 = \frac{16\pi \gamma^3}{3 \dot{p}^2}, \quad (\text{S8})$$

$$\zeta_{2\text{D}} = \zeta_{3\text{D}} h(\theta). \quad (\text{S9})$$

With the time-dependent free energy barrier given by Eq. S7, S6 has the closed-form solution

$$I(t) = t \exp \left[ - \left( \frac{\zeta}{t} \right)^2 \right] - \sqrt{\pi} \zeta \operatorname{erfc} \left( \frac{\zeta}{t} \right), \quad (\text{S10})$$

where  $\operatorname{erfc}(x)$  is the complementary error function. The mean cavitation time in the pressure-ramp protocol follows as

$$\tau = - \int_0^\infty t \dot{f}(t) dt = \int_0^\infty f(t) dt. \quad (\text{S11})$$

Defining the dynamic cavitation pressure in the pressure-ramp protocol as  $p_{\text{cav}}^* = \dot{p} \tau$ , one finds

$$p_{\text{cav}}^* = \dot{p} \int_0^\infty e^{-k_0 I(t)} dt. \quad (\text{S12})$$

During a simulation, we apply a negative pressure rate  $\dot{p} < 0$  (i.e., the pressure is decreasing) and identify  $p_{\text{cav}}^*$ , the pressure at which cavitation occurs. Simulating several rates allows us to fit Eq. S12, where the kinetic prefactor  $k_0$  is the only fitting parameter.

### S3. FITTING $\kappa_{2D}(\theta)$

To fit the data for  $\kappa_{2D}(\theta)$  in Fig. 3D in the main text, we use the following fitting function,

$$\kappa_{2D}(\theta) = \kappa_{2D,0} \exp \left[ \sum_{p=1}^4 (\theta/\theta_p)^p \right]. \quad (\text{S13})$$

The fit yields  $\kappa_{2D,0} = 1.93 \times 10^{-35} \text{ ns}^{-1} \text{ nm}^{-2}$ ,  $\theta_1 = 0.21^\circ$ ,  $\theta_2 = 3.70^\circ$ ,  $\theta_3 = 12.61^\circ$ , and  $\theta_4 = 29.77^\circ$ . The resulting fit is shown as a solid line in Figs. 2D and S2A and was used in the subsequent analysis in the main text.

We also examine the implications of using a fitting function with a quadratic polynomial in the exponent for the subsequent analysis, given by

$$\kappa_{2D}(\theta) = \kappa_{2D,0} \exp \left[ \sum_{p=1}^2 (\theta/\theta_p)^p \right]. \quad (\text{S14})$$

This fit, plotted as a dashed black line in Fig. S2A does not match the data as well as the fourth-order polynomial fit. More critically, when we compute the resulting crossover contact angle  $\theta^*$  (using Eq. 11), shown in Fig. S2B, this quadratic fit predicts  $\theta^*$  below  $45^\circ$  for small box sizes  $L$ . This result is in contradiction with the simulation outcome for a contact angle of  $45^\circ$ , where cavitation in the bulk water phase occurs. Therefore, a fit limited to second order does not adequately extrapolate to small contact angles.

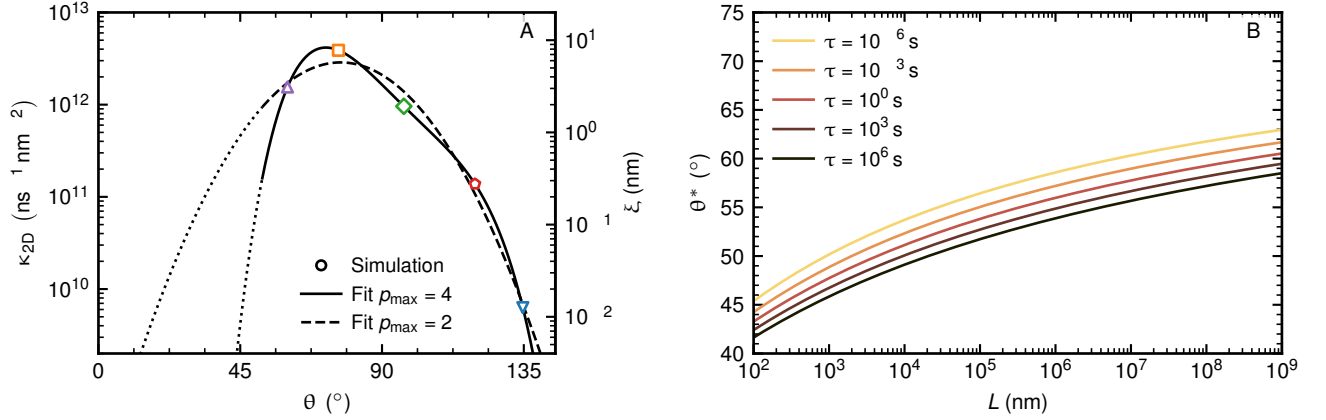


Figure S2. (A) Fit of Eq. S13 (solid line, as in Fig. 3D in the main text) and Eq. S14 (dashed line) to the  $\kappa_{2D}$  data points from simulations. As in the main text the fits for  $\theta < 52^\circ$  are shown as dotted lines. (B) Crossover contact angle  $\theta^*$  as a function of container size  $L$  for different waiting times  $\tau$ . Similar to Fig. 4B, but here based on the fit of Eq. S14 in Eq. 11.

### S4. CAVITATION PRESSURE FOR VARIOUS WAITING TIMES $\tau$

In Fig. S3, we present the cavitation pressure as a function of contact angle, similar to Fig. 4A in the main text, but for considerably shorter (Fig. S3 A) and longer (Fig. S3 B) waiting times. We find that increasing  $\tau$  leads to a less negative cavitation pressure  $p_{\text{cav}}$  and a lower crossover contact angle  $\theta^*$  at which the cavitation transits from bulk to surface. The latter trend is also quantified in Fig. 4B.

### S5. ANALYTIC ESTIMATE FOR THE CROSSOVER CONTACT ANGLE $\theta^*$

We derive an approximate expression for the crossover contact angle  $\theta^*$ , which follows from Eq. 11 in the main text. Taking the logarithm of both sides of Eq. 11 gives

$$\ln L = \frac{1}{3h(\theta^*) - 2} [\ln(6\kappa_{2D}\tau) - h(\theta^*) \ln(\kappa_{3D}\tau)] \quad (\text{S15})$$



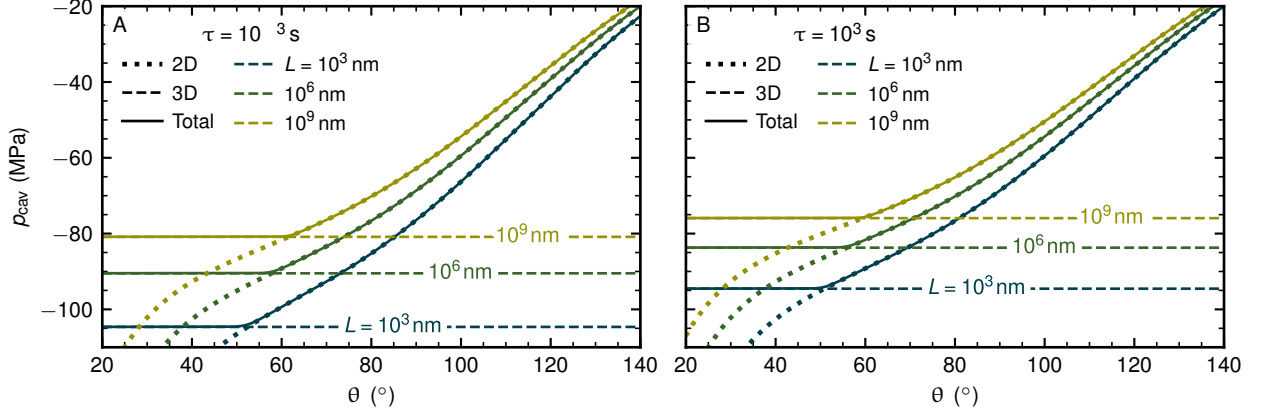


Figure S3. Cavitation pressure  $p_{\text{cav}}$  as a function of contact angle  $\theta$ , similar to Fig. 4A in the main text, here shown for waiting times of (A)  $\tau = 10^{-3}$  s and (B)  $\tau = 1000$  s  $\approx 17$  min.

from which  $h(\theta^*)$  follows as

$$h(\theta^*) = \frac{\ln(6\kappa_{2D}L^2\tau)}{\ln(\kappa_{3D}L^3\tau)}. \quad (\text{S16})$$

By expressing  $\kappa_{2D}$  in terms of  $\xi = \kappa_{2D}/\kappa_{3D}$ , we obtain

$$h(\theta^*) = 1 + \frac{\ln(6\xi/L)}{\ln(\kappa_{3D}L^3\tau)}. \quad (\text{S17})$$

Next, we perform a Taylor expansion of the geometric function  $h(\theta^*)$ , given by Eq. 8, for small angles, which approximates as  $h(\theta) \simeq 1 - \frac{3}{16}\theta^4$ . Substituting this into Eq. S17 leads to the final expression

$$\theta^* \approx \left\{ \frac{16 \ln[(L/(6\xi))]}{3 \ln(\kappa_{3D}L^3\tau)} \right\}^{1/4}, \quad (\text{S18})$$

which is Eq. 12 in the main text.

---

[1] M. Kanduč and R. R. Netz, Atomistic simulations of wetting properties and water films on hydrophilic surfaces, *The Journal of Chemical Physics* **146**, 164705 (2017).